NANO LETTERS

pubs.acs.org/NanoLett Letter

Overcoming the Heat Transfer Paradox: Nano Ridges Induce "Pistol Bubbles" and Reverse the Boiling Curve

Jinliang Xu, Wenli Ye, Xiongjiang Yu,* and Bo Zhang

Cite This: https://doi.org/10.1021/acs.nanolett.3c03337 Read Online

ACCESS | Metrics & More | Article Recommendations | Supporting Information

ABSTRACT: To increase the boiling heat transfer limit, we disrupted the previously nonevaporating region and increased the vaporization activity of "inert" liquid molecules by introducing nano ridges on the boiling surface. This solved the paradox of no heat transfer occurring through the thinnest liquid film in boiling bubbles; thus, the internal heat transfer limit of the bubbles was exceeded. We found that vigorous boiling occurred immediately once the nonevaporating region was activated, and the bubble frequency increased by an order of magnitude, reaching 1186 Hz, which has not been previously reported. With an increase in heat flux, the boiling curve exhibited a "return". We achieved an extremely high bubble frequency by experimentally quantifying the major influence of nonevaporating region disruption on boiling heat transfer. The mechanism behind the generation of the ultrahigh-frequency bubbles was discovered. This study also reveals a new mechanism for the reversed boiling curve.

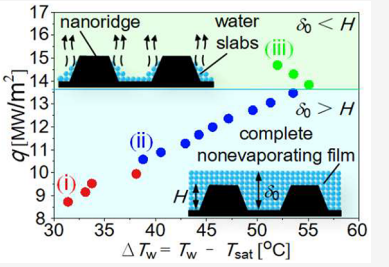

KEYWORDS: *nanostructure ridges, bubble frequency, inertia growth, nonevaporating film, boiling curve*

Since the proposal of pool boiling heat transfer, it has been widely applied in various engineering applications such as nuclear reactors, heat exchangers, aerospace electronic equipment, electronic devices, and other high heat flux devices.[1−8] Several factors can improve pool boiling effectiveness, such as increased surface area,[9] nucleation site density,[10] wettability,[11] reduced instability wavelength,[12] and capillary core suction or spreading.[13] These factors for improving pool boiling are primarily related to macroscopic or microscopic aspects, and further research on nanoscale fundamental problems regarding heat transfer inside a boiling bubble is required. The three-phase contact line occurring at the bottom of a bubble represents the interface between the liquid−vapor and solid surface. The contact line region dynamics determine the growth and departure of bubbles, providing valuable insights into the phenomenon of boiling.[14] The contact line is generally believed to be divided into three regions:[15,16] the nonevaporating film (nanoscale), the evaporating film (microscale), and the intrinsic meniscus (milliscale). Based on the liquid film heat transfer coefficient (h_l) equation ($h_l = k_l/\delta_l$), since liquid thermal conductivity (k_l) is constant, h_l increases as the liquid film thickness (δ_l) decreases. Therefore, the thinnest nonevaporating film region should have the highest heat transfer potential. However, adhesion forces prevent the nonevaporating film from evaporating, giving rise to the paradox that "no heat transfer occurs through the thinnest liquid film." As a result, the heat transfer potential of the nonevaporating film remains untapped. Although Wayner et al.[17] initially proposed the lack of heat transfer in the nonevaporating film, further research has revealed that the nonevaporating film can significantly affect the overall macroscopic heat transfer.[18] Owing to the complex dynamics of bubbles and testing conditions, a few experiments[16,19−21] and molecular dynamics simulations[22−24] have addressed the formation and characteristics of the nonevaporating film.

Microelectromechanical systems (MEMS)[25] provide potential technological support in studying the characteristics of nanoscale nonevaporating films because one can fabricate a microheater with nanoscale thickness, which is comparable to the thickness of nonevaporating films, using standard sputtering techniques. In previous literature, the bubble frequency generated on the microheater was rarely >200 Hz (see Table S1 in the Supporting Information), which was considerably lower than the bubble frequency observed in the current study, i.e., 1186 Hz. Smaller bubble sizes were found to correspond to higher frequency and lower thermal resistance,[26] which caused rapid cooling of the wall surface and the occurrence of a "reversed" boiling curve, demonstrating the full potential of heat transfer enhancement through the nonevaporating film. Our experiment also revealed that the entire lifecycle of a bubble, including nucleation, growth, and collapse, can be completed within a very short time period of ∼0.2 ms. This process is analogous to the quick loading and shooting of a pistol; thus, we name the bubbles "pistol bubbles". Theoretical analysis further validated that the majority of bubble growth occurred during the fast-growing

Received: September 2, 2023
Revised: October 17, 2023
Accepted: October 17, 2023

https://doi.org/10.1021/acs.nanolett.3c03337
Nano Lett. XXXX, XXX, XXX−XXX

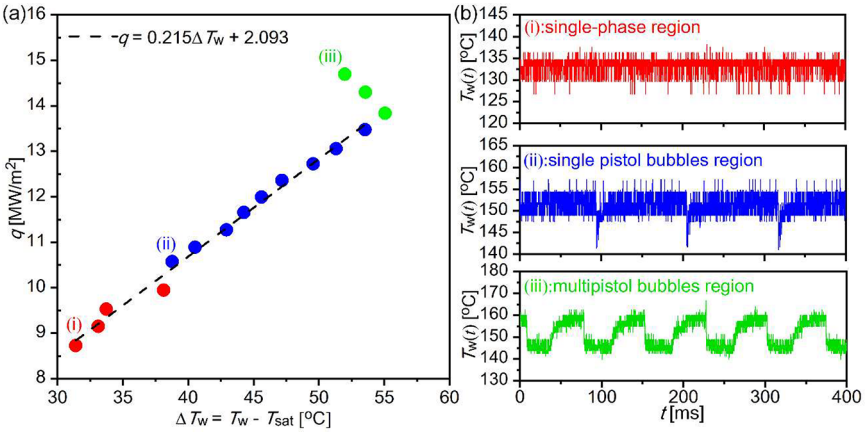

Figure 1. Three heat transfer regions on the nanoridged surface: (a) reversed boiling curve and (b) transient wall temperature fluctuations for (i) the single-phase region, (ii) the single pistol bubbles region, and (iii) the multipistol bubbles region.

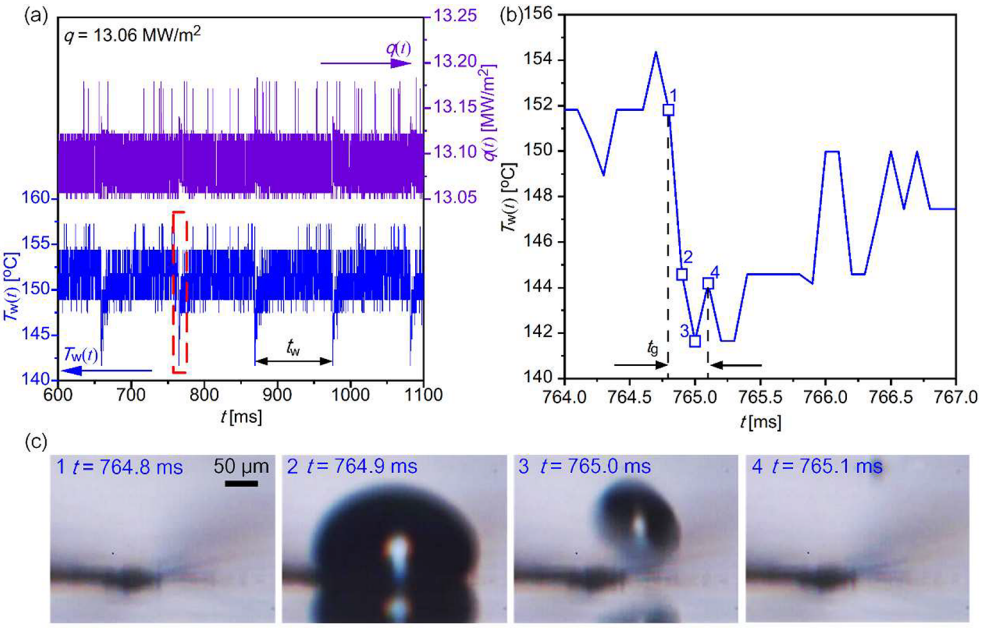

Figure 2. (a) Transient parameter fluctuations at q = 13.06 MW/m^2, (b) detailed wall temperature fluctuations at 764−767 ms, and (c) corresponding visual images at 764.8−765.1 ms.

inertia-controlled regime. Owing to the faster growth rates, boiling heat transfer is more efficient in the inertia-controlled regime than in the heat-transfer-controlled regime.[27] Finally, a quantitative link between the trigger for the fast pistol bubbles and the breakup of the nonevaporating film is established.

Within the range of the heat flux q = 0−15 MW/m^2, there were three heat transfer modes (Figure 1a), where the x-axis represents the wall superheat $\Delta T_w = T_w - T_{sat}$ and T_w is the wall temperature and T_{sat} is the saturation temperature. The transient wall temperature (T_w(t)) of the microheater varied in each mode, as shown in Figure 1b. (i) In the single-phase region, ΔT_w increased with anncrease in q. During a heating time of 0−400 ms, T_w(t) did not vary substantially and no bubbles were generated during the heating process. (ii) In the single pistol bubbles region, ΔT_w similarly increased with the increase in q. However, within the same heating period, there were several abrupt decreases in T_w(t) of a very short duration (~0.4 ms), showing clear periodicity. The abrupt decreases in T_w(t) corresponded to the generation of big bubbles, followed by a recovery to the average value. (iii) In the multipistol bubbles region, ΔT_w decreased instead of rising with the increase in q. Within the same heating period, periodic abrupt reductions and recoveries in T_w(t) were observed, similar to the single pistol bubbles region. However, the duration of the lower T_w(t) values was longer, and alternating occurrences of large and small bubbles could be observed.

The heat transfer efficiency in the multipistol bubble region differed from those of the previous two regions. As shown in Figure 1a, the boiling curve in this heat transfer region exhibited a return, which is usually called secondary boiling or boiling inversion.[28,29] Researchers believe that this phenomenon occurs because of the activation of more nucleation sites at a high heat flux or the establishment of liquid−vapor separation pathways, facilitating the detachment of bubbles. However, no reports have been found that establish a connection between this phenomenon and the rupture of nanoscale nonevaporating films. The following section establishes a mathematical model for the nonevaporating film

https://doi.org/10.1021/acs.nanolett.3c03337
Nano Lett. XXXX, XXX, XXX−XXX

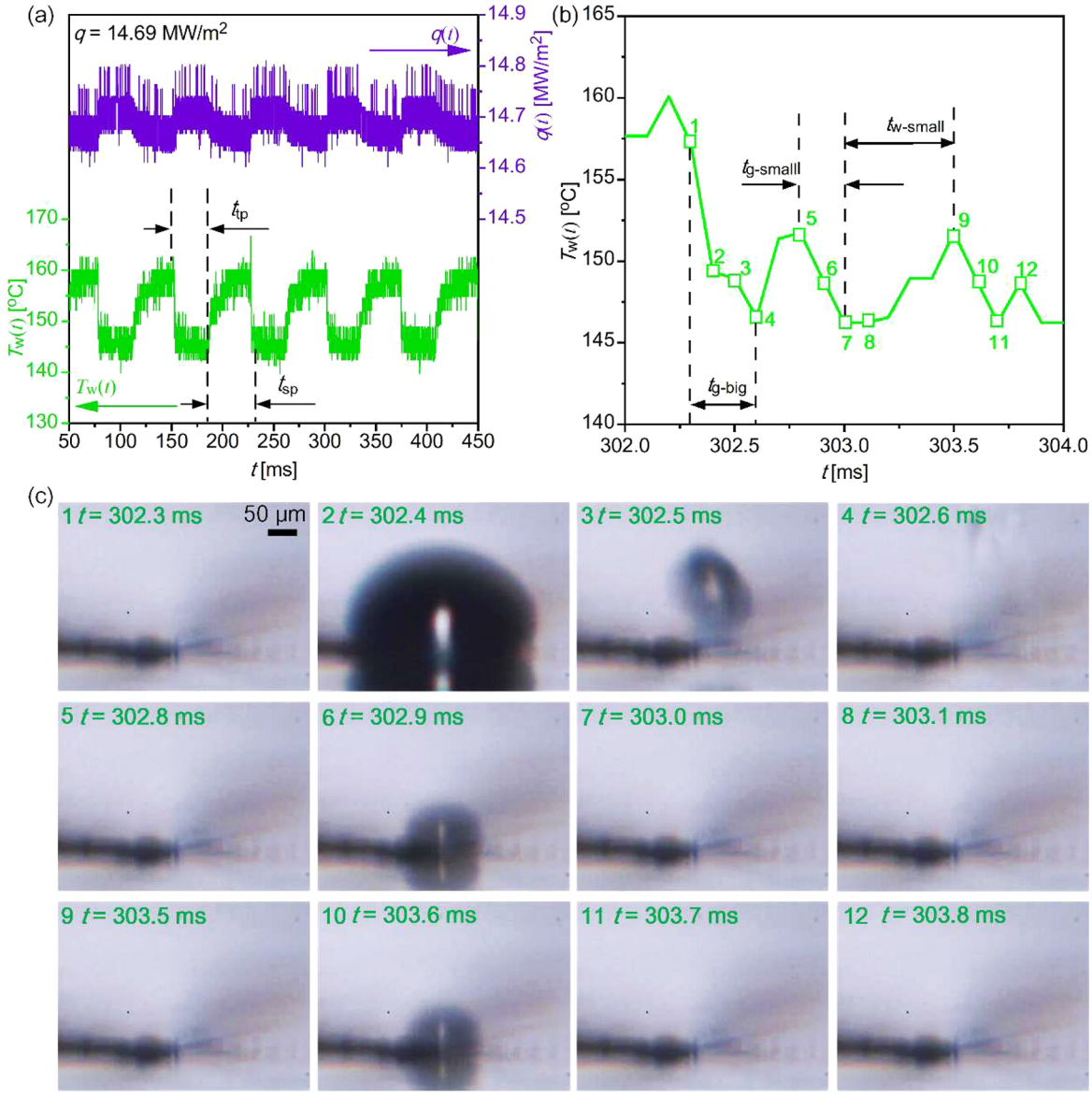

Figure 3. (a) Transient parameter fluctuations at q = 14.69 MW/m^2, (b) detailed wall temperature fluctuations at 302−304 ms, and (c) corresponding visual images of the changes at 302.3−303.8 ms.

thickness and quantitatively analyzes the relationship between the film thickness and ridges height within this region, intending to find a criterion of the occurrence of the "reversal" in the boiling curve and reveal a new mechanism for boiling heat transfer.

As an example, Figure 2a shows the $T_w(t)$ values for q = 13.06 MW/m^2 in the single pistol bubbles region. The moment when $T_w(t)$ decreased corresponded to the increase in the transient heat flux ($q(t)$). At the same bubble nucleation point, a certain time interval was required for a bubble to depart with the formation of the next bubble. This time interval is termed the waiting time (t_w). The nucleation and growth of the bubble until the collapse also require a certain time interval, which is called the growth time (t_g). Figure 2b shows a local magnification of the $T_w(t)$ fluctuations within the period of 764−767 ms. The t_g value of the bubble was 0.4 ms. The reciprocal of the sum of t_w and t_g is the bubble frequency (f). The visual images in Figure 2c further confirm the rapid growth and detachment of bubbles: the moment of bubble appearance (t = 764.9 ms) corresponded to the minimum value of $T_w(t)$. The bubble nucleation was not observed at t = 764.8 ms. However, the maximum bubble growth was observed in the next frame (t = 764.9 ms), and the bubble detachment and collapse were completed at t = 765.0 ms and t = 765.1 ms, respectively. After the collapse is completed, there is no immediate generation of the next bubble. Heat transfer entered a relatively long t_w, during which energy accumulated for generation of the next bubble. The time interval between the appearances of the two bubbles was ∼111.2 ms (Video S1 can be found in the Supporting Information).

In the multipistol bubble region with alternating big and small bubbles, using the condition of q = 14.69 MW/m^2 as an example, Figure 3a shows $T_w(t)$ and $q(t)$. Unlike the single pistol bubble region, the $T_w(t)$ fluctuation exhibited a two-phase time (t_{tp}) (78.5−112.9 and 153.4−187.4 ms) and a single-phase time (t_{sp}) (113−153 and 187.5−227.8 ms). t_{tp} produced a large number of small bubbles with very high frequency, whereas t_{sp} represented the time between the

https://doi.org/10.1021/acs.nanolett.3c03337
Nano Lett. XXXX, XXX, XXX−XXX

disappearance of the last small bubble and the appearance of the first big bubble. During this t_{sp}, $T_w(t)$ slowly increased. Figure 3b shows a magnified view of the $T_w(t)$ fluctuations from 302 to 306 ms, displaying the growth time of the big bubble ($t_{g\text{-}big}$), the growth time of the small bubble ($t_{g\text{-}small}$), and the waiting time of the small bubble ($t_{w\text{-}small}$). The definitions of $t_{g\text{-}small}$ and $t_{w\text{-}small}$ are the same as those of t_g and t_w in the single pistol bubbles region. Figure 3c shows visual images of this condition. The moment when the big bubble appeared (t = 302.4 ms) corresponded to the beginning of the t_{tp}. Similar to the single pistol bubbles region, the nucleation, growth, and collapse of the big bubble were completed in ~0.4 ms. However, unlike the single pistol bubbles region, after the collapse of the big bubble, a large number of small bubbles were generated within ~0.5 ms at the same location where the previous big bubbles were formed, with an extremely high frequency (~1000 Hz). Furthermore, $t_{g\text{-}small}$ and $t_{w\text{-}small}$ were shorter than t_g and t_w. When the generation of small bubbles ceased, the heating state entered t_{sp}, during which energy was accumulated for the generation of the next big bubble. The time interval between the appearances of the two big bubbles was ~70.0 ms. (See Sections S6 and S7 of the Supporting Information for the statistical results of the bubbles or Video S2 for original recordings.)

When bubbles are small, the bubble growth is in the inertia-controlled regime, where the growth is rapid and is limited by the inertial force of the surrounding liquid.[30] Inertia-controlled growth is restricted to the initial stages of expansion, when the bubble growth rate is primarily determined by its ability to accelerate or "push back" the surrounding liquid, independent of the rate of vapor generation in the bubble. For this case, the bubble growth could be predicted by solving the momentum equation alone. Assuming potential flow, integration of the one-dimensional momentum equation in the liquid provides an expression that describes the growth of the bubble according to eq 1.[31,32]

$$\frac{P_v - P_b}{\rho_l} = R\frac{d^2R}{dt^2} + \frac{3}{2}\left(\frac{dR}{dt}\right)^2 + \frac{2\sigma}{\rho_l R} \quad (1)$$

where P_v is the vapor pressure inside the bubble, P_b is the bulk liquid pressure, ρ_l is the liquid density, R is the bubble radius, and σ is the surface tension. The pressure rise across the vapor−liquid interface is related by the Young−Laplace equation $P_v - P_b = 2\sigma/R$. Equation 1, known as the extended or modified Rayleigh equation, is an equilibrium balance among the pressure of the vapor, the surface tension stresses, and the net pressure imposed by the liquid. Integration of eq 1, assuming the vapor pressure is nearly constant at $P_v = P_{sat}$ (saturated pressure) and the bubble is large enough that the surface tension term is negligible, yields the Rayleigh solution for inertial controlled growth

$$t_{inertia} = R(t)/\left(\frac{2}{3}\left[\frac{T_\infty - T_{sat}}{T_{sat}}\right]\frac{h_{fg}\rho_v}{\rho l}\right)^{1/2} \quad (2)$$

where $P_v - P_b$ is replaced by the linearized Clapeyron equation $P_v - P_b = \frac{\rho_v h_{fg}}{T_{sat}}(T_\infty - T_{sat})$. T_∞ is the liquid temperature around the bubble, h_{fg} is the latent heat of vaporization, and ρ_v is the vapor density.

Equation 2 is derived from a homogeneous liquid−vapor phase change process because boiling incipience on the microheater is precisely a homogeneous liquid−vapor phase change process.[33] Before nucleation of the bubble, T_w is very high, and T_w instantly decreases after nucleation, where T_w before nucleation can be regarded as the superheated liquid temperature around the bubble with a diameter of 0 (T_∞ in eq 2). For the single pistol bubble region, T_w is taken as the average value of T_w (t) within t_w. For the multipistol bubble region, the big bubble T_w is taken as the value of $T_w(t)$ within t_{sp}, and the small bubble T_w is taken as the average value of $T_w(t)$ within t_{tp}. The corresponding bubble inertia growth time ($t_{inertia}$) can be calculated using eq 2 to be 0.17−0.24 ms for the single pistol bubble region and 0.09−0.11 ms for smaller bubbles in the multipistol bubble region. Because the collapse of bubbles occurred within a time scale similar to that of the inertia growth process,[34] the sum of $t_{inertia}$ and the collapse time was $t_g \approx 2t_{inertia}$. t_g ranges from 0.34 to 0.48 ms for single pistol bubbles and from 0.18 to 0.22 ms for smaller bubbles in the multipistol bubble region, which are consistent with our experiment results (see Figures 2c and 3c for examples). We assume that boiling incipience on the microheater is a homogeneous liquid−vapor phase change process and the top of the bubble reaches the edge of the thermal boundary layer before collapse. As small bubbles appear, the thermal boundary layer thickness decreases and is assumed to be equal to the radius of the small bubbles. The theoretical result can be calculated from the t_w calculation (eq 3;[35] hollow squares in Figure 4)

$$t_w = \frac{\delta_{th}^2}{\pi\alpha_l} = \frac{\bar{D}^2}{2\pi\alpha_l} \quad (3)$$

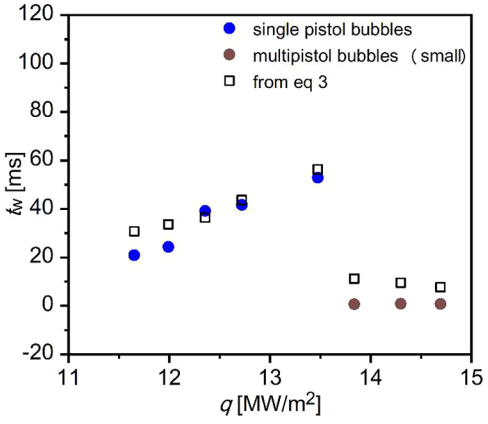

Figure 4. Waiting time of bubble generation decreases sharply when entering the multipistol bubble region.

where δ_{th} is the thermal boundary layer thickness, α_l is the liquid thermal diffusivity, and $\bar{D}$ is the bubble average diameter. By comparing the classical theoretical calculations with the experimental data, we conclude that small bubbles in the multipistol bubble region lead to a reduction in δ_{th} and a shorter t_w, eventually causing an increase in the bubble frequency.

As mentioned previously, the contact line at the base of the bubble can be divided into three regions (Figure 5a). Initially, the evaporating film approaches the wall with a practical curvature of slope $K = K_{bubble}$, which defines the intrinsic static contact angle θ. The evaporating film in this region has essentially the same curvature as the intrinsic meniscus in the

https://doi.org/10.1021/acs.nanolett.3c03337
Nano Lett. XXXX, XXX, XXX−XXX

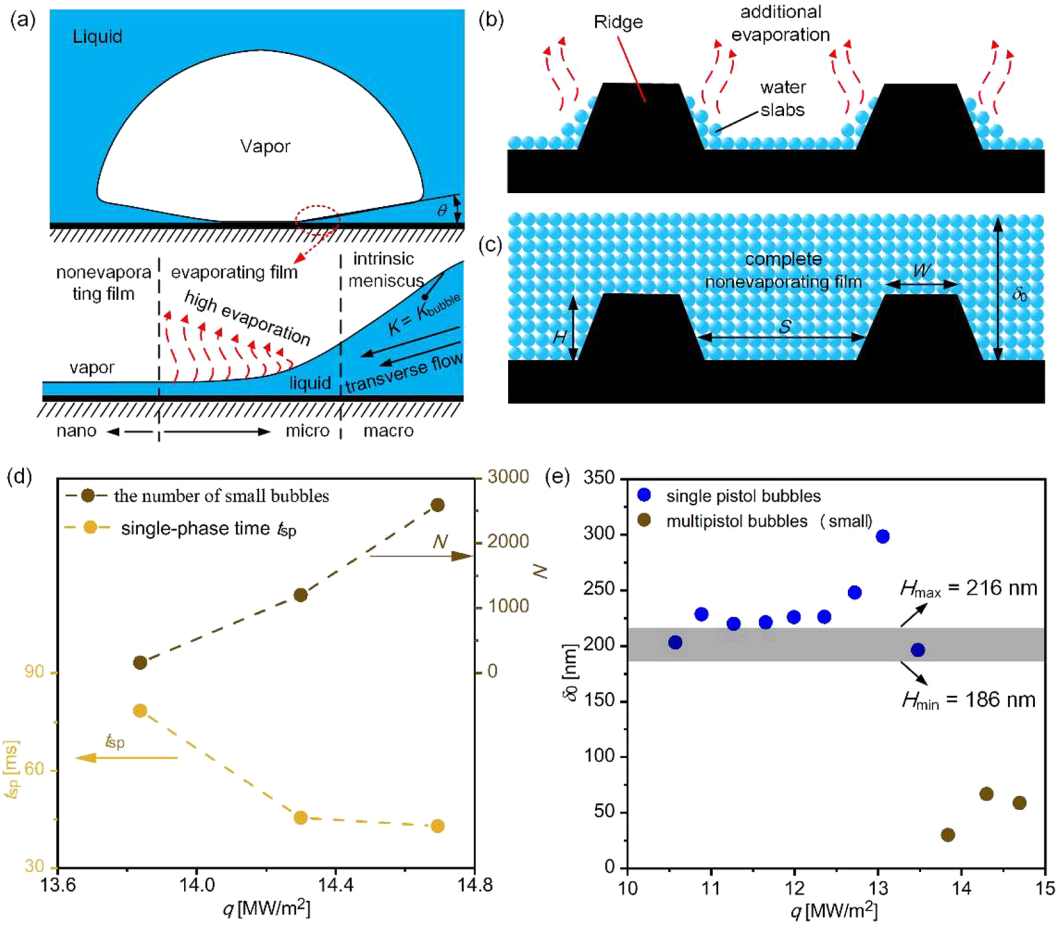

Figure 5. (a) Three regions underneath a boiling bubble near the contact line: nonevaporating film, evaporating film, and intrinsic meniscus. (b) Additional evaporation when the ridge height H is higher than the nonevaporating film thickness δ_0. (c) A complete nonevaporating film when H is lower than the δ_0. (d) Variations of number of small bubbles and single-phase time t_{sp} with heat flux q. (e) Variation of δ_0 with q.

macro region. The transition region occurs between the nonevaporating and evaporating films, and the liquid film varies in thickness and curvature to accommodate the transition between the two regions. This is the thinnest portion of the meniscus over which the highest evaporation can occur.[36] The high evaporation rates in the micro region then create a significant transverse liquid flow. In the micro region where the meniscus approaches the wall, the short-range attractive forces between the liquid molecules and the wall atoms become significant, producing an adhesion pressure in the liquid. The adhesion pressure tends to steadily reduce the interface curvature in the flow direction until the meniscus levels out at the end of the micro region, forming a stationary nonevaporating film. Here, we introduce solid nano ridges to manipulate this liquid film. When the ridge height (H) is greater than the nonevaporating film thickness (δ_0), the film breaks into independent slabs of water between the ridges (Figure 5b). The curvature of the water slabs is greater than that of the complete nonevaporating film (Figure 5c) because of the additional hydrophilic ridge surface−water force. Therefore, the curvature of the nonevaporating region increases, the evaporation pressure decreases, and the liquid molecules in the nonevaporating region are activated.

The relationship between δ_0 and H determines the generation of small bubbles in the multipistol bubble region. Once the H overcomes δ_0, the negative slope of the boiling curve and appearance of small bubbles show up in the multipistol bubble region. A greater number of small bubbles (N) and shorter t_{sp} (Figure 5d) lead to a stronger cooling effect for the microheater wall, accounting for the negative slope. Since H can be obtained by a Bruker Contour GT-K-Elite instrument (Germany), we should know δ_0 to make a quantitative comparison. By modifying the Mikic and Rohsenow[37] model after coupling the nonevaporating film heat transfer mechanism, the relevant equations are obtained as[16,19]

$$q = \frac{2\pi k_l (T_w - T_{sat})}{\sqrt{\pi \alpha_l}} \mathrm{Na}[\bar{D}^2 \sqrt{f_{ne} f}] \tag{4}$$

$$\mathrm{Na} = \left[25 \times 10^{-8} \left(\frac{h_{fg} \rho_v (T_w - T_{sat})}{T_{sat} \sigma}\right)^{1.5}\right]^2 \tag{5}$$

$$f_{ne} = \frac{V_b}{V_b - V_{ne}} \tag{6}$$

$$V_b = \frac{\pi}{6}\left(\frac{\bar{D}}{2} + \frac{\bar{D}}{2}\cos\theta\right)\left[3\left(\frac{\bar{D}}{2}\right)^2 \sin^2\theta + \left(\frac{\bar{D}}{2} + \frac{\bar{D}}{2}\cos\theta\right)^2\right] \tag{7}$$

https://doi.org/10.1021/acs.nanolett.3c03337
Nano Lett. XXXX, XXX, XXX−XXX

$$V_{ne} = \frac{2\rho_l \pi (r_{ne})^2 \delta_0}{M_{H_2O}} \cdot \frac{S}{S+W} \cdot \frac{R_g T_{sat}}{P_b + 4\sigma/\bar{D}} \tag{8}$$

where k_l is the liquid thermal conductivity, Na is the nucleation site density, f_{ne} is the nonevaporating film factor, V_b is the hemispherical bubble volume, V_{ne} is the equivalent vapor volume of the nonevaporating film beneath the bubble, M_{H_2O} is the molecular mass of water, R_g is the ideal gas constant, r_{ne} is the nonevaporating film spread radius, δ_0 is the nonevaporating film thickness, W is the ridge width, and S is the ridge spacing. Thus, δ_0 is obtained by combining eq 4−8 as follows:

$$\delta_0 = V_b \cdot \left[1 - \frac{4f\pi^2 k_l^2 (T_w - T_{sat})^2 Na^2 \bar{D}^4}{q^2 \pi \alpha_l}\right] \cdot \frac{M_{H_2O}}{2\rho_l \pi (r_{ne})^2} \cdot \frac{S+W}{W} \cdot \frac{P_b + 4\sigma/\bar{D}}{R_g T_{sat}} \tag{9}$$

Zhao et al.[38] developed an expression for the r_{ne} as a function of t_g, which expanded upon the theoretical and experimental analysis of microlayer growth proposed by Cooper and Lloyd[39]

$$r_{ne} = \left[\frac{8 c_{pl} k_l^2 (T_w - T_{sat})^3 (t_g - t_{ne})}{(C_{ne}\mathrm{Pr})^2 \alpha_l h_{fg}^3 \rho_v^2}\right]^{1/2} \tag{10}$$

$$t_{ne} = \left[\frac{\sqrt{C_{ne}\mathrm{Pr}\alpha_l}\rho_v h_{fg} \bar{D}}{4k_l (T_w - T_{sat})}\right]^2 \tag{11}$$

where c_{pl} is the specific heat of the liquid, Pr is the Prandtl number, t_{ne} is the microlayer formation time, and C_{ne} is the correction factor (for boiling on the microheater, C_{ne} = 0.1156).[40]

The result from eq 9 was obtained, as shown in Figure 5e. The gray blocks represent the range of the ridge height. In the single pistol bubble region, the calculated results almost all fell above the gray blocks, demonstrating that $\delta_0 > H$. At this time, the nonevaporating film was not destroyed into independent liquid blocks with curvature, and according to the aforementioned nonevaporating film theory, no additional evaporation occurred on the intact noncurvature nonevaporating film. However, in the multipistol bubble region, the calculated results all fell below the gray block, demonstrating that $\delta_0 < H$. The flat superheated liquid inside the nonevaporating film was broken into separate liquid blocks by the microheater ridges, and the liquid blocks formed curvature at the "slope" because of the wetting nature of microheater trapezoidal ridges. The separate liquid blocks in the nonevaporating region could generate additional evaporation at the slope. Thus, the heat transfer potential in the nonevaporating region was stimulated, resulting in a large number of small bubbles under high heat flux, a long period of low wall superheat in $T_w(t)$ fluctuations, and a negative slope of the boiling curve.

In summary, we realized a new heat transfer mechanism using nanoridges to disrupt the previously nonevaporating region and achieve the highest bubble frequency to the best of the authors' knowledge. Our work opens a new way of micro/nano scale thermal management as well as bubble regulation using nanotechnologies.

■ ASSOCIATED CONTENT

Supporting Information

The Supporting Information is available free of charge at https://pubs.acs.org/doi/10.1021/acs.nanolett.3c03337.

Bubble behavior on the single pistol bubble region (MP4)

Bubble behavior on the multipistol bubble region (MP4)

Further information about test section fabrication, calibration, experimental setup, data reduction, error analysis, growth time and frequency of bubbles, and bubble diameter (PDF)

■ AUTHOR INFORMATION

Corresponding Author

Xiongjiang Yu − *The Beijing Key Laboratory of Multiphase Flow and Heat Transfer for Low Grade Energy Utilization, North China Electric Power University, Beijing 102206, People's Republic of China;* orcid.org/0000-0003-2156-7420; Email: yuxiongjiang@ncepu.edu.cn

Authors

Jinliang Xu − *The Beijing Key Laboratory of Multiphase Flow and Heat Transfer for Low Grade Energy Utilization, North China Electric Power University, Beijing 102206, People's Republic of China;* orcid.org/0000-0003-0145-9983

Wenli Ye − *The Beijing Key Laboratory of Multiphase Flow and Heat Transfer for Low Grade Energy Utilization, North China Electric Power University, Beijing 102206, People's Republic of China*

Bo Zhang − *The Beijing Key Laboratory of Multiphase Flow and Heat Transfer for Low Grade Energy Utilization, North China Electric Power University, Beijing 102206, People's Republic of China*

Complete contact information is available at: https://pubs.acs.org/10.1021/acs.nanolett.3c03337

Author Contributions

X.Y. and W.Y. conceived the initial idea for this research. J.X. guided the work. W.Y. and B.Z. prepared and characterized the experimental samples. X.Y., W.Y., and B.Z. carried out the pool boiling experiments and analyzed the data. W.Y. and X.Y. carried out the theoretical analysis. W.Y. and X.Y. wrote the manuscript.

Notes

The authors declare no competing financial interest.

■ ACKNOWLEDGMENTS

The authors acknowledge support from the National Natural Science Foundation of China (52206197, 52130608) and the Fundamental Research Funds for the Central Universities (2023MS014).

■ REFERENCES

(1) Li, C.; Wang, Z.; Wang, P. I.; Peles, Y.; Koratkar, N.; Peterson, G. Nanostructured copper interfaces for enhanced boiling. *Small.* **2008**, *4* (8), 1084−1088.

(2) Chen, R.; Lu, M.-C.; Srinivasan, V.; Wang, Z.; Cho, H. H.; Majumdar, A. Nanowires for enhanced boiling heat transfer. *Nano Lett.* **2009**, *9* (2), 548−553.

(3) Cho, H. J.; Mizerak, J. P.; Wang, E. N. Turning bubbles on and off during boiling using charged surfactants. *Nat. Commun.* **2015**, *6* (1), 8599.
(4) Dhillon, N. S.; Buongiorno, J.; Varanasi, K. K. Critical heat flux maxima during boiling crisis on textured surfaces. *Nat. Commun.* **2015**, *6* (1), 8247.
(5) Cho, H. J.; Preston, D. J.; Zhu, Y.; Wang, E. N. Nanoengineered materials for liquid−vapour phase-change heat transfer. *Nat. Rev. Mater.* **2017**, *2*, 16092.
(6) Wen, R.; Li, Q.; Wang, W.; Latour, B.; Li, C. H.; Li, C.; Lee, Y.-C.; Yang, R. Enhanced bubble nucleation and liquid rewetting for highly efficient boiling heat transfer on two-level hierarchical surfaces with patterned copper nanowire arrays. *Nano Energy.* **2017**, *38*, 59−65.
(7) Shin, S.; Choi, G.; Rallabandi, B.; Lee, D.; Shim, D. I.; Kim, B. S.; Kim, K. M.; Cho, H. H. Enhanced boiling heat transfer using self-actuated nanobimorphs. *Nano Lett.* **2018**, *18* (10), 6392−6396.
(8) Li, J.; Fu, W.; Zhang, B.; Zhu, G.; Miljkovic, N. Ultrascalable three-tier hierarchical nanoengineered surfaces for optimized boiling. *ACS Nano* **2019**, *13* (12), 14080−14093.
(9) Ji, X.; Xu, J.; Zhao, Z.; Yang, W. Pool boiling heat transfer on uniform and non-uniform porous coating surfaces. *Exp.Therm. Fluid Sci.* **2013**, *48*, 198−212.
(10) Yang, Y.; Ji, X.; Xu, J. Pool boiling heat transfer on copper foam covers with water as working fluid. *Int. J. Therm Sci.* **2010**, *49* (7), 1227−1237.
(11) Ji, X.; Xu, J.; Li, H.; Huang, G. Switchable heat transfer mechanisms of nucleation and convection by wettability match of evaporator and condenser for heat pipes: Nano-structured surface effect. *Nano Energy.* **2017**, *38*, 313−325.
(12) Xu, J.; Yu, X.; Jin, W. Porous-wall microchannels generate high frequency "eye-blinking" interface oscillation, yielding ultra-stable wall temperatures. *Int. J. Heat Mass Transfer* **2016**, *101*, 341−353.
(13) Yu, X.; Xu, J.; Liu, G.; Ji, X. Phase separation evaporator using pin-fin-porous wall microchannels: Comprehensive upgrading of thermal-hydraulic operating performance. *Int. J. Heat Mass Transfer* **2021**, *164*, No. 120460.
(14) Stephan, P.; Hammer, J. A new model for nucleate boiling heat transfer. *Heat and Mass Transfer.* **1994**, *30* (2), 119−125.
(15) Gerardi, C.; Buongiorno, J.; Hu, L.-w.; McKrell, T. Study of bubble growth in water pool boiling through synchronized, infrared thermometry and high-speed video. *Int. J. Heat Mass Transfer* **2010**, *53* (19−20), 4185−4192.
(16) Zou, A.; Maroo, S. C. Critical height of micro/nano structures for pool boiling heat transfer enhancement. *Phys. Lett.* **2013**, *103* (22), 221602.
(17) Wayner, P., Jr; Kao, Y.; LaCroix, L. The interline heat-transfer coefficient of an evaporating wetting film. *Int. J. Heat Mass Transfer* **1976**, *19* (5), 487−492.
(18) Stephan, P.; Busse, C. Analysis of the heat transfer coefficient of grooved heat pipe evaporator walls. *Int. J. Heat Mass Transfer* **1992**, *35* (2), 383−391.
(19) Zou, A.; Singh, D. P.; Maroo, S. C. Early evaporation of microlayer for boiling heat transfer enhancement. *Langmuir.* **2016**, *32* (42), 10808−10814.
(20) Jaikumar, A.; Gupta, A.; Kandlikar, S. G.; Yang, C.-Y.; Su, C.-Y. Scale effects of graphene and graphene oxide coatings on pool boiling enhancement mechanisms. *Int. J. Heat Mass Transfer* **2017**, *109*, 357−366.
(21) Jaikumar, A.; Rishi, A.; Gupta, A.; Kandlikar, S. G. Microscale morphology effects of copper−graphene oxide coatings on pool boiling characteristics. *J. Heat Transfer.* **2017**, *139* (11), 111509.
(22) Maroo, S. C.; Chung, J. Nanoscale liquid-vapor phase-change physics in nonevaporating region at the three-phase contact line. *J. Appl. Phys.* **2009**, *106* (6), No. 064911.
(23) Duursma, G.; Jiang, F.; Sefiane, K.; Duff, S.; Beji, H. On the effects of thermocapillary driven oscillations on bubble growth during boiling of FC-72 on a thin wire. *Int. J. Therm Sci.* **2011**, *50* (10), 1809−1819.
(24) Maroo, S. C.; Chung, J. A possible role of nanostructured ridges on boiling heat transfer enhancement. *J. Heat Transfer.* **2013**, *135* (4), No. 041501.
(25) Judy, J. W. Microelectromechanical systems (MEMS): fabrication, design and applications. *Smart Mater. Struct.* **2001**, *10* (6), 1115.
(26) Wang, Q.; Chen, R. Widely tunable thin film boiling heat transfer through nanoporous membranes. *Nano Energy.* **2018**, *54*, 297−303.
(27) Wang, Q.; Chen, R. Ultrahigh Flux Thin Film Boiling Heat Transfer Through Nanoporous Membranes. *Nano Lett.* **2018**, *18* (5), 3096−3103.
(28) Kruse, C.; Tsubaki, A.; Zuhlke, C.; Anderson, T.; Alexander, D.; Gogos, G.; Ndao, S. Secondary pool boiling effects. *Appl. Phys. Lett.* **2016**, *108* (5), No. 051602.
(29) Jaikumar, A.; Kandlikar, S. Pool boiling inversion through bubble induced macroconvection. *Appl. Phys. Lett.* **2017**, *110* (9), No. 094107.
(30) Robinson, A.; Judd, R. The dynamics of spherical bubble growth. *Int. J. Heat Mass Transfer* **2004**, *47* (23), 5101−5113.
(31) Plesset, M. S.; Zwick, S. A. The growth of vapor bubbles in superheated liquids. *J. Appl. Phys.* **1954**, *25* (4), 493−500.
(32) Forster, H.; Zuber, N. Dynamics of vapor bubbles and boiling heat transfer. *AIChE J.* **1955**, *1* (4), 531−535.
(33) Chen, T.; Klausner, J. F.; Garimella, S. V.; Chung, J. N. Subcooled boiling incipience on a highly smooth microheater. *Int. J. Heat Mass Transfer* **2006**, *49* (23−24), 4399−4406.
(34) Zuber, N. The dynamics of vapor bubbles in nonuniform temperature fields. *Int. J. Heat Mass Transfer* **1961**, *2* (1−2), 83−98.
(35) Chi-Yeh, H.; Griffith, P. The mechanism of heat transfer in nucleate pool boiling—Part I: Bubble initiaton, growth and departure. *Int. J. Heat Mass Transfer* **1965**, *8* (6), 887−904.
(36) Maroo, S. C.; Chung, J. Fundamental roles of nonevaporating film and ultrahigh heat flux associated with nanoscale meniscus evaporation in nucleate boiling. *J. Heat Transfer.* **2013**, *135* (6), No. 061501.
(37) Mikic, B. B.; Rohsenow, W. M. A New Correlation of Pool-Boiling Data Including the Effect of Heating Surface Characteristics. *J. Heat Transfer.* **1969**, *91* (2), 245−250.
(38) Zhao, Y.-H.; Masuoka, T.; Tsuruta, T. Unified theoretical prediction of fully developed nucleate boiling and critical heat flux based on a dynamic microlayer model. *Int. J. Heat Mass Transfer* **2002**, *45* (15), 3189−3197.
(39) Cooper, M.; Lloyd, A. The microlayer in nucleate pool boiling. *Int. J. Heat Mass Transfer* **1969**, *12* (8), 895−913.
(40) Yabuki, T.; Nakabeppu, O. Microlayer formation characteristics in pool isolated bubble boiling of water. *Heat and Mass Transfer.* **2017**, *53*, 1745−1750.

https://doi.org/10.1021/acs.nanolett.3c03337
Nano Lett. XXXX, XXX, XXX−XXX